https://doi.org/10.5194/essd-2022-167
Preprint. Discussion started: 31 May 2022

Open Access Earth System Science Data Discussions

A newly integrated ground temperature dataset of permafrost along the China-Russia crude oil pipeline route in Northeast China

Guoyu Li[1,3,4], Wei Ma[1,3,4], Fei Wang[1, 2*], Huijun Jin[1, 3, 5*], Fedorov Alexander[6], Dun Chen[1,3], Gang Wu[1,3,4], Yapeng Cao[1,3,4], Yu Zhou[1,3,4], Yanhu Mu[1,3,4], Yuncheng Mao[7], Jun Zhang[8], Kai Gao[1,3,4], Xiaoying Jin[5], Ruixia He[1,3], Xinyu Li[9], and Yan Li[1,3]

[1] State Key Laboratory of Frozen Soil Engineering, Northwest Institute of Eco-Environment and Resources, Chinese Academy of Sciences, Lanzhou 730000, China;
[2] Faculty of Civil Engineering and Mechanics, Jiangsu University, Zhenjiang 212013, China;
[3] Da Xing'anling Observation and Research Station of Frozen-Ground Engineering and Environment, Northwest Institute of Eco-Environment and Resources, Chinese Academy of Sciences, Jagdaqi, Inner Mongolia 165000, China;
[4] School of Engineering Science, University of Chinese Academy of Sciences, Beijing 100049, China;
[5] School of Civil Engineering and Institute of Cold Regions Science and Engineering, Northeast Forestry University, Harbin 150040, China;
[6] Melnikov Permafrost Institute, Russian Academy of Sciences, Yakutsk 677010, Russia;
[7] School of Civil Engineering, Northwest Minzu University, Lanzhou 730000, China;
[8] School of Civil Engineering, Henan Polytechnic University, Jiaozuo 454000, China, and;
[9] School of Civil Engineering, Harbin Institute of Technology, Harbin 150090, China

Correspondence: Fei Wang (wangfei9107@ujs.edu.cn) and Huijun Jin (hjjin@nefu.edu.cn)

Abstract: The thermal state of permafrost in the present and future is fundamental to the ecosystem evolution, hydrological process, carbon release, and infrastructure integrity in cold regions. From 2011, we began to establish a permafrost monitoring network along the China-Russia crude oil pipelines (CRCOPs) route at the eastern flank of the northern Da Xing'anling Mountains in Northeast China. Based on meteorological data near the southern limit of latitudinal permafrost (SLLP), ground temperature data in 20 boreholes with the depths of 10–60.6 m, soil volumetric liquid water contents and 2-D electrical resistivity tomography (ERT) data, we compiled an integrated dataset of the ground thermal state along the CRCOPs route. Study results demonstrate that permafrost in the vicinity of SLLP has experienced marked warming (2011–2020) to climate change, manifested as the rising permafrost temperatures at depth. Local thermal disturbances triggered by the construction and operation of CRCOPs have resulted in significant permafrost warming and subsequent thawing on the right-of-way (ROW) of the pipeline. This permafrost thaw will persist, but it can be alleviated by adopting mitigative measures, such as insulation layer and thermosyphons. The in-situ observational dataset is of great value for assessing the variability of permafrost under the linear disturbances of the CRCOPs and related environmental effects, for understanding hydro-thermal-mechanical interactions between

https://doi.org/10.5194/essd-2022-167
Preprint. Discussion started: 31 May 2022

the buried pipelines and permafrost foundation soils, and for evaluating the operational and structural integrity of the pipeline systems in the future. The dataset is available at the National Tibetan Plateau/Third Pole Environment Data Center (http://doi.org/10.11888/Cryos.tpdc.272357; Li, 2022).

https://doi.org/10.5194/essd-2022-167
Preprint. Discussion started: 31 May 2022

1 Introduction

As a major component of the cryosphere, the thermal state of permafrost is sensitive to climate change, surface disturbances and human activities (Smith et al., 2022). Over the last few decades, the warming and thawing of permafrost have been observed in most permafrost regions (e.g., Osterkamp and Romanovsky, 1999; Harris et al., 2003; Isaksen et al., 2007; Wu and Zhang, 2008; Ran et al., 2018; Biskaborn et al., 2019), and permafrost degradation will continue in response to a warming climate (Zhang et al., 2008; Koven et al., 2013). Permafrost change affects the geomorphological characteristics, carbon release, hydrological process, ecosystem, climate system, and integrity of infrastructure (Nelson et al., 2001; Schuur et al., 2009; Cheng and Jin, 2013; Beck et al., 2015; Hjort et al., 2018, 2022; Turetsky et al., 2020; Jin and Ma, 2021; Jin et al., 2021, 2022; Luo et al., 2021; Jones et al., 2022; Liu et al., 2022; Miner et al., 2022).

Permafrost occurs extensively in the Da and Xiao Xing'anling mountains in Northeast China (referred to as the Xing’an permafrost). Its distribution displays both latitudinal and altitudinal zonality and is strongly influenced by local environmental factors (Jin et al., 2008; Guo et al., 2018; He et al., 2021). The Xing’an permafrost has also experienced significant degradation under climate warming, wildfire, and human activities including deforestation, urbanization, mining and linear infrastructure construction (Guo and Li, 1981; Jin et al., 2007; Wang et al., 2019a; Mao et al., 2019; Li et al., 2021; Serban et al., 2021), as evidenced by rising ground temperature (GT), thickening active layer, shrinking permafrost extent, and increasing thaw-related hazards, such as ground surface subsidence, settlement of foundation soils and development of taliks and thermokarst. Multiple studies on future changes in Xing’an permafrost have been conducted based on different modeling approaches and climate warming scenarios (e.g., Ran et al., 2012; Zhang et al., 2021). Research results indicate that persistent permafrost degradation is likely to occur during the next few decades (Jin et al., 2007; Wei et al., 2011). However, there are great uncertainties in the prediction of the magnitude and timing of these changes (Smith et al., 2022). For example, the estimated areal extent

https://doi.org/10.5194/essd-2022-167
Preprint. Discussion started: 31 May 2022

of existing permafrost in Northeast China ranges from 2.4×10^5 to 3.1×10^5 km^2 (Ran et al., 2012; Zhang et al., 2021). Field observations of meteorological variables and permafrost thermal states have substantially contributed to the understanding of the responses of GTs to climate change and hydrothermal processes in the active layer and permafrost, facilitating the evaluation and/or validation of predictive permafrost models, and thus they are of great importance (Zhao et al., 2021; Wu et al., 2022). However, in Northeast China, long-term and continuous datasets of permafrost thermal state are scarce, especially at the eastern flank of the Da Xing'anling Mountains, due to the harsh periglacial environment, inconvenient access, and expensive installation and maintenance costs (Jin et al., 2007; He et al., 2021; Li et al., 2021).

Since 2008, extensive permafrost investigations for the construction of the China-Russia crude oil pipelines (CRCOPs) I and II were conducted in the permafrost zones on the eastern slopes of the Da Xing'anling Mountains. As a result, a permafrost monitoring network along the CRCOPs route was gradually established through the joint efforts of the State Key Laboratory of Frozen Soils Engineering (SKLFSE) of the Chinese Academy of Sciences and the PetroChina Pipeline Company. In addition to the measurements of GTs in the active layer and near-surface permafrost on and off the right-of-way (ROW) of the CRCOPs in boreholes, the electrical resistivity tomography (ERT) was used to detect the boundary of the permafrost and talik (thawed bulb/cylinder) around the CRCOPs. Farzamian et al. (2020) also conducted ERT surveys to detect the ground freeze-thaw dynamics in the active layer. Based on GTs in boreholes and inverted ERT results, the shapes and sizes of talik around the CRCOPs have been delineated. Meanwhile, a meteorological station was established near the southern limit of Xing'an permafrost (50.47°N and 124.23°E, 484 m a.s.l.).

We firstly present the integrated dataset of permafrost thermal state along the CRCOPs route on the eastern slopes of the northern Da Xing'anling Mountains, in Northeast China. This dataset includes meteorological data, GTs, soil volumetric liquid water content, and subsurface electrical resistivity (ER) on and off the ROW of the pipeline. Detailed information for the integrated dataset is provided so that this dataset can be easily understood, accessed and

https://doi.org/10.5194/essd-2022-167
Preprint. Discussion started: 31 May 2022

79 applied by potential users.

80 2 Study site and instruments

81 Five permafrost observation sites, named as Xing'an (XA), Xin-tian (XT), Jin-song (JS), Song-ling (SL), and Jagdaqi
82 Bei (North) (JB), respectively, are established along the CRCOPs route in Northeast China (50.47°–53.33°N,
83 123.99°–124.31°E) (Fig.1) through the joint efforts of the SKLFSE and the PetroChina Pipeline Company. Site
84 selection is primarily based on engineering geological conditions of permafrost (Jin et al., 2010). According to the
85 meteorological data of 1972–2017, the study area is characterized of a frigid-temperate continental monsoon climate
86 with mean annual air temperatures (MAAT) of −4.0 to −0.4 °C, with annual precipitation of 447 to 525 mm, which
87 falls mostly as summer rain. Snow cover generally occurs at the end of September–beginning of October and
88 disappears in late April and early May of next year. The snow depth ranges from 5 to 35 cm. From 1972 to 2017,
89 MAAT was rising at a linear average rate of 0.32 °C per decade while annual precipitation increased with a linear
90 average rate of climate wetting at 14.6 mm per decade (Wang et al., 2019a). Table 1 summarizes the geographical
91 information and permafrost characteristics of monitoring sites retrieved from both data described in this paper and
92 previous publications. The mean annual ground temperature (MAGT) at the depth of zero annual amplitude (D_{ZAA})
93 ranges from −1.8 to −0.4 °C, indicating a warm permafrost (Harris et al., 2017). The permafrost thickness exceeds
94 60 m, and the observed active layer thickness (ALT) ranges from 1.0 to 2.7 m (Wang et al., 2019b). The XA site is
95 located in a permafrost wetland with the highest latitude and coldest air temperature, while the JB site, near the
96 southern limit of the latitudinal permafrost (SLLP) in Northeast China and with the lowest latitude and the highest
97 air temperature, displays the characteristics of an isolated patches plermafrost zone. The XT and JS sites are located
98 in the transition zone between isolated patches of permafrost and sporadic permafrost, making them the ideal
99 locations for examining permafrost dynamics. The SL site is located in a wetland underlain by ice-saturated and ice-
100 rich permafrost, where a seasonal frost mound with a maximum height of 2 m is developed (Wang et al., 2015), and

https://doi.org/10.5194/essd-2022-167
Preprint. Discussion started: 31 May 2022

Open Access Earth System Science Data Discussions

101 monitoring devices are prone to be destroyed due to significant frost mound-related ground deformation.

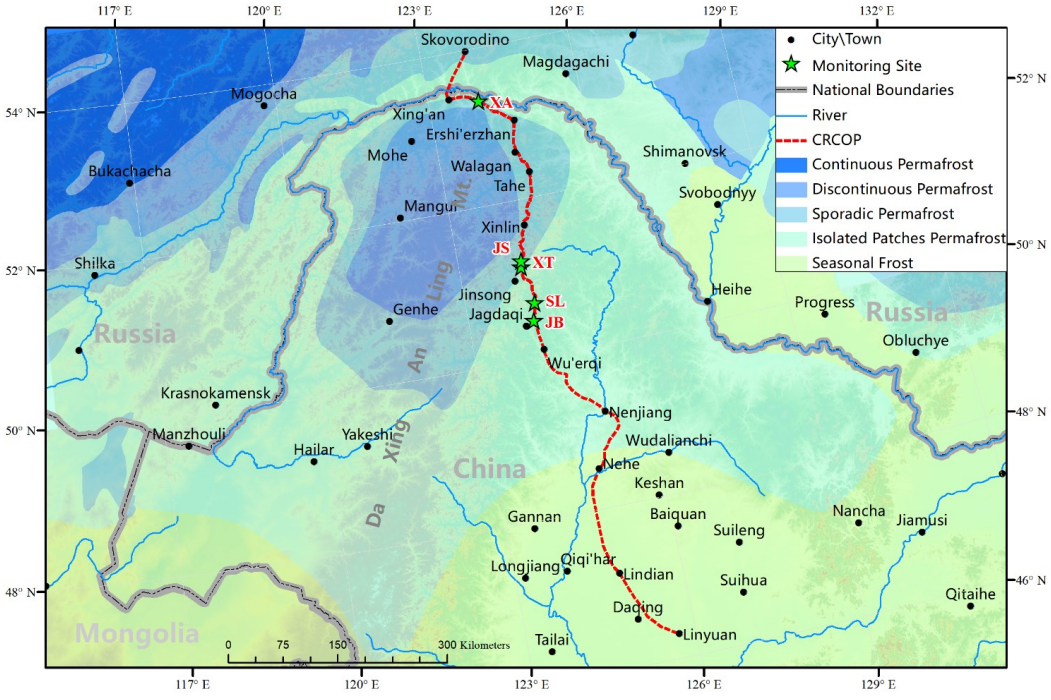

102

103 Figure 1. Location of permafrost monitoring sites along the route of the CRCOPs. Permafrost zones are derived from the
104 International Permafrost Association (IPA) map (Brown et al., 1998). The red dash line represents the paralleling CRCOPs
105 I and II (the inter-pipeline distance is generally limited to approximately 10 m).

106 Table 1. Permafrost characteristics for monitoring sites along the route of CRCOPs.

Site	Lat. (°N)	Long. (°E)	Elev. (m a.s.l.)	Permafrost zone	Vegetation	Ice content	MAGT (°C)	ALT (cm)
XA	53.33	123.99	318	Sporadic permafrost	*Carex tato swamp*	Ice-saturated	−1.8	130
XT	51.24	124.21	621	Sporadic permafrost	*Shrub meadow*	Ice-saturated	−1.8	100
JS	51.16	124.19	508	Sporadic permafrost	*Carex tato swamp*	Ice-rich	−0.7 to −0.4	200~270
SL	50.69	124.31	398	Isolated patches permafrost	*Carex tato swamp*	Ice-saturated /ice-rich	−0.9	130
JB	50.47	124.23	484	Isolated patches permafrost	*Carex tato swamp*	Ice-rich	−0.8 to −0.5	178~200

107 Notes: MAGT, mean annual ground temperature, and ALT, active layer thickness.

108 In October 2017, a small automated weather station (AWS, Fig.B1) was built at the JB site for measuring air
109 temperature, relative humidity, wind speed and direction, and total solar radiation. Details of the sensors used are
110 listed in Table 2. Near the AWS, a 60.6-m deep temperature borehole (drilled during the cold season when the active

https://doi.org/10.5194/essd-2022-167
Preprint. Discussion started: 31 May 2022


Open Access Earth System Science Data Discussions

111 layer was frozen up and finished more than 6 months before AWS installation) was set up simultaneously to record
112 the temperature of the active layer and permafrost. All monitoring data were recorded every 2 h by a CR3000 data
113 logger (Campbell Scientific, Inc. USA) with a relay multiplexer (TRM128, China), powered by a battery cell and
114 solar panel regulated by a solar charge controller (Phocos ECO (10 A), Germany). The collected data have been
115 transferred automatically to the specified server by the wireless transmission module (HKT-DTU, Campbell
116 Scientific, Inc., USA). Using such technology (i.e., online data transmission) it would be possible to check collected
117 data in real-time and identify possible sensor failures.

118 In total, there are 20 boreholes drilled and instrumented for GT monitoring both on the ROW of the CRCOPs
119 and at the nearby undisturbed sites (off the ROW) between 2011 and 2021. The depths of boreholes range from 10 to
120 60.6 m, although most of them are 15 to 20 m deep (Table 3). In-situ temperature monitoring in the borehole JB-B-
121 II was deployed starting in November 2011, and additional ten boreholes were drilled in 2014 and 2015 at the JB site
122 (Table 3). At the SL site, three boreholes of 25 m in depth were drilled at horizontal distances of 3.0, 5.9, and 24.4 m
123 vertically from the centerline of the CRCOP I in March 2017 and instrumented in September 2017. At the JS site,
124 two boreholes on the ROW of the pipeline were established in 2017, and an additional borehole was drilled at the
125 nearby undisturbed site in 2018. A borehole at the XT site, 10 km north of the JS site, was drilled in 2019 to evaluate
126 the spatial differentiation of permafrost distribution influenced by local geo-environmental factors. At the XA site, a
127 borehole with a depth of 60.5 m was drilled 7 km south of the first pump station of the CRCOPs in Mo'he County,
128 Heilongjiang Province, where there was previously no GT data. The GTs in the borehole was measured by a
129 thermistor cable (assembled by the SKLFSE), in which thermistors were arranged at the designed intervals (Table 2).
130 Manual temperature reading using Fluke 87/89 had been made in five boreholes (SL-B-I, SL-B-1, SL-B-2, JB-B-II,
131 and JB-B-1) for some time. Two types of data loggers, which are connected to the thermistor cables, are now used
132 for automatic and continuous GTs monitoring in boreholes. They are CR3000 data loggers and miniature temperature
133 data loggers. The miniature temperature data logger (RTB37a36V3, jointly developed by Northwestern Polytechnical

https://doi.org/10.5194/essd-2022-167
Preprint. Discussion started: 31 May 2022

University and SKLFSE) generally has poorer accuracy than the CR3000 data logger, but allows more widely used due to its lower cost. The GT in boreholes at the SL site has been recorded by this miniature data logger. The soil volumetric liquid water content (VWC) was measured by the Campbell Scientific CS616 water content reflectometer probe (Table 2) by connecting to a CR3000 data logger. Three pits were excavated at 20-m intervals longitudinally near the CRCOP I at the JB site and three probes were embedded horizontally at depths of 0.5, 1.5, and 2.5 m in each pit (Table 3).

The ER is dependent on many parameters including lithology, water/ice content, and soil temperature. The ER distribution in the subsurface can be visualized by ERT, which provides a continuous transect of the active layer and permafrost characteristics to delineate the shape and size of the talik or permafrost island along the CRCOPs route. We performed ERT surveys in April 2018 with the SuperSting R8 system (Advanced Geosciences, Inc., Table 2) using the Wenner-Schlumberger configuration due to its high signal-to-noise ratio (Dahlin and Zhou, 2014). In addition to the fourth ERT profile at the JB site (P-JB-4), other profiles are done using stainless electrodes spaced by 2 m along the 120-m-long profile, reaching a maximum penetration depth of 24 m (Table 3). The smoothness-constrained least-squares method is employed for ERT inversion.

https://doi.org/10.5194/essd-2022-167
Preprint. Discussion started: 31 May 2022

Open Access Earth System Science Data Discussions

148 Table 2 List of sensors, measuring range and accuracy for meteorological data, ground temperature, soil water content, and
149 ground resistivity.

Variable	Sensor/measurement device	Measuring range (operating temperature)	Accuracy
Meteorological data			
Air temperature	HMP155A Vaisala Finland	−80 to 60 ℃	(0.226-0.0028×*T*)℃ (−80 to 20℃), (0.055+0.0057×*T*)℃ (20 to 60 ℃)
Relative humidity (RH)	HMP155A Vaisala Finland	0 to 100% RH	(1.4+0.032×RH)% (−60 to −40℃), (1.2+0.012×RH)% (−40 to −20℃, 40 to 60℃), (1.0+0.008×RH)% (−20 to 40℃)
Wind speed/direction	Model 05103 R.M. Young Company	0 to 100 m/s (−50 to 50℃)	±0.3 m s^{-1}, ±3°
Total solar radiation	LI200X Pyranometer Campbell Scientific, Inc.	0~1000 W/m^2 (−40 to 65℃)	±5% (absolute error in natural daylight), ±3% typical
Permafrost monitoring			
Soil temperature	Thermistor cable SKLFSE, China	−30 to 30 ℃	±0.05℃
Soil volumetric liquid water content	CS616 Campbell Scientific, Inc.	0% to saturation (0 to 70℃)	±2.5%
Ground electrical resistivity	SuperSting R8 system Advanced Geosciences, Inc.	−10 to 10 V	⩽30nV

150

https://doi.org/10.5194/essd-2022-167
Preprint. Discussion started: 31 May 2022

Open Access Earth System Science Data Discussions

151 Table 3 Summary of monitoring information of ground temperature boreholes, water content pits, and ERT profiles along
152 the CRCOPs in Northeast China.

Variable	Borehole/ ERT profile	Monitoring depth (m)	Measuring internal	Operation period
Soil/permafrost temperature at the natural site	XA-B-I	0.5, 1, 1.5, 2, 2.5, 3, 3.5, 4.5, 5.5, 6.5, 7.5, 8.5, 9.5, 10.5, 11.5, 13.5, 14.5, 15.5, 16.5, 17.5, 18.5, 19.5, 20.5, 22.5, 24.5, 26.5, 28.5, 30.5, 32.5, 34.5, 36.5, 38.5, 40.5, 42.5, 44.5, 46.5, 48.5, 50.5, 52.5, 54.5, 56.5, 58.5, 60.5	2h, AUTO	Nov 2018 – Nov 2020
	XT-B-I	0, 0.5, 1, 1.5, 2, 2.5, 3, 3.5, 4, 5, 6, 7, 8, 9, 10, 11, 12, 13, 14, 15, 16, 17, 18, 19, 20	2h, AUTO	Jul 2019 – Aug 2021
	JS-B-I	0, 0.5, 1, 1.5, 2, 2.5, 3, 4, 5, 6, 7, 8, 9, 10, 11, 12, 13, 14, 15, 16, 17, 18, 19, 20	2h, AUTO	Dec 2018 – Jun 2021
	SL-B-I	0, 0.5, 1, 1.5, 2, 2.5, 3, 3.5, 4, 5, 6, 7, 8, 9, 10, 11, 12, 13, 14, 15, 16, 17, 18, 19, 20, 21, 22, 23, 24, 25	Monthly, MANU 2h, AUTO	Sep 2017 – Oct 2019 Aug 2020 – Dec 2020
	JB-B-I	0.6, 1.1, 1.6, 2.1, 2.6, 3.1, 3.6, 4.6, 5.6, 6.6, 7.6, 8.6, 9.6, 10.6, 11.6, 12.6, 13.6, 15.6, 16.6, 17.6, 18.6, 19.6, 20.6, 22.6, 24.6, 26.6, 28.6, 30.6, 32.6, 34.6, 36.6, 38.6, 40.6, 42.6, 44.6, 46.6, 48.6, 50.6, 52.6, 54.6, 56.6, 58.6, 60.6	2h, AUTO	Jun 2018 – Aug 2020
	JB-B-II	0, 0.5, 1, 1.5, 2, 2.5, 3, 3.5, 4, 4.5, 5, 6, 7, 8, 9, 10, 11, 12, 13, 14, 15, 16, 17, 18, 19, 20	Monthly, MANU 2h, AUTO	Nov 2011 – Sep 2017 Oct 2017 – Aug 2021
Soil/permafrost temperature on pipeline ROW	JS-B-1	0.3, 0.8, 1.3, 1.8, 2.3, 2.8, 3.3, 3.8, 4.8, 5.8, 6.8, 7.8, 8.8, 9.8, 10.8, 11.8, 12.8, 13.8, 14.8, 15.8, 16.8, 17.8, 18.8, 19.8	2h, AUTO	Oct 2017 – May 2021
	JS-B-2	0, 0.5, 1, 1.5, 2, 2.5, 3, 3.5, 4, 5, 6, 7, 8, 9, 10, 11, 12, 13, 14, 15, 16, 17, 18, 19, 20	2h, AUTO	Oct 2017 – Aug 2021
	SL-B-1	0.3, 0.8, 1.3, 1.8, 2.3, 2.8, 3.3, 3.8, 4.8, 5.8, 6.8, 7.8, 8.8, 9.8, 10.8, 11.8, 12.8, 13.8, 14.8, 15.8, 16.8, 17.8, 18.8, 19.8, 20.8, 21.8, 22.8, 23.8, 24.8	Monthly, MANU 2h, AUTO	Sep 2017 – Oct 2019 Aug 2020 – May 2021
	SL-B-2			
	JB-B-1	0, 0.5, 1, 1.5, 2, 2.5, 3, 3.5, 4, 5, 6, 7, 8, 9, 10, 11, 12, 13, 14, 15, 16, 17, 18, 19, 20	Monthly, MANU 2h, AUTO	Mar 2014 – Sep 2017 Oct 2017 – Aug 2021
	JB-B-2	0, 0.5, 1, 1.5, 2, 2.5, 3, 3.5, 4, 5, 6, 7, 8, 9, 10, 11, 12, 13, 14, 15	2h, AUTO	Jun 2015 – Aug
	JB-B-3			Jun 2015 –
	JB-B-4			Jun 2015 –
	JB-B-5	0, 1, 2, 3, 4, 5, 6, 7, 8, 9, 10		Jun 2015 – Aug
	JB-B-6	0, 0.5, 1, 1.5, 2, 2.5, 3, 4, 5, 6, 7, 8, 9, 10, 11, 12, 13, 14		Jun 2015 –
	JB-B-7			Jun 2015 –
	JB-B-8	0, 0.5, 1, 1.5, 2, 2.5, 3, 3.5, 4, 5, 6, 7, 8, 9, 10, 11, 12, 13, 14, 15		Jun 2015 – Aug
	JB-B-9			Jun 2015 –
	JB-B-10			Jun 2015 –
Soil volumetric liquid water content	JB-W1 JB-W2 JB-W3	0.5,1.5,2.5	2h, AUTO	Jun 2015–Aug 2021
Electrical resistivity	P-JS	0.5, 1.5, 2.6, 3.7, 5.0, 6.4, 7.9, 9.6, 11.5, 13.5, 15.8, 18.2, 21.0, 24.0	Site visit	Apr 11, 2018
	P-SL	0.5, 1.5, 2.6, 3.7, 5.0, 6.4, 7.9, 9.6, 11.5, 13.5, 15.8, 18.2, 21.0, 24.0	Site visit	Apr 12, 2018
	P-JB-1			
	P-JB-2	0.5, 1.5, 2.6, 3.7, 5.0, 6.4, 7.9, 9.6, 11.5, 13.5, 15.8, 18.2, 21.0, 24.0	Site visit	Apr 06 – Apr 10, 2018
	P-JB-3			
	P-JB-4	0.4, 1.1, 1.9, 2.8, 3.7, 4.8, 5.9, 7.2, 8.6, 10.1, 11.8, 13.7, 15.7, 18.0		

https://doi.org/10.5194/essd-2022-167
Preprint. Discussion started: 31 May 2022

3 Data description

3.1 Meteorological data

The AWS at the JB site was regularly maintained and repaired, resulting in a data collection with satisfactory quality and continuity. Between 15 October 2017 and 10 August 2020, less than 5% of the data were missing. However, the meteorological data had been discontinued since 10 August 2020, due to the failure of the online data transmission module and lack of essential on-site maintenance for equipment under the influence of the COVID-19 pandemic.

Air temperature and relative humidity were measured at a height of 1.5 m every two hours using the Vaisala HMP155A sensor protected by a radiation shield. The accuracy of temperature and relative humidity measurements decreased along with the temperature drops. For example, the accuracy for the HMP155A sensor at 20 °C was 0.17 °C, but it reached up to 0.34 °C at −40 °C (Table 2). At the JB permafrost site, the annual range of daily air temperature was approximately 56 °C. The recorded maximum air temperature was 24.7 °C on 25 July 2020, and the minimum, −33.7 °C on 27 December 2019 (Fig. 2a). The seasonal variation of relative humidity was consistent with the seasonal variability in air temperature (Fig. 2b).

Total solar radiation was also measured at a height of 1.5 m above the ground surface by the LI200X Pyranometer with an accuracy of ±3% to ±5% (Table 2). Although the sensor was regularly checked (e.g. checking the level of the instrument, removing dust) during the site visits and re-calibrated after two years of installation, it was largely unattended and its accuracy was therefore likely to exceed ±5%. It is worth noting that the LI200X may read negative solar radiation during the night, which is later set to zero in the data processing. The total solar radiation reached its maximum in summer (June to August) and was lowest in winter (December to next February), with a similar pattern with seasonal variations in air temperature (Fig. 2c).

The wind speed and direction were measured at a height of 2 m above the ground surface by a propeller anemometer (Model 05103, R.M. Young Company, Table 2). The standard error of wind direction was also calculated

https://doi.org/10.5194/essd-2022-167
Preprint. Discussion started: 31 May 2022

using a specific algorithm provided by the CR3000 data logger. The recorded maximum wind speed of 9 m s^{-1}occurred on 28 May 2019. The average monthly wind speed ranged from 0.9 to 2.6 m s^{-1} and reached its maximum in April–May.

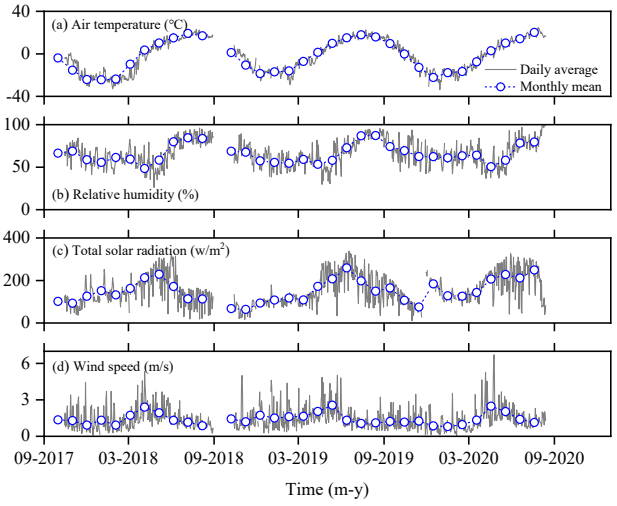

Figure 2. Time series of meteorological variables at the JB site from October 2017 to August 2020.

3.2 Ground temperature at the undisturbed sites

The GT measurements were carried out by installing a thermistor cable protected by the steel tube into the borehole (Wang et al., 2019b). To analyze the GT spatial distribution, we chose GTs between 2018 and 2021, when GT data series of all five permafrost sites were available (Fig. 3). The average daily GTs in the active layer (at depths of 0–3 m) showed seasonal dynamic variations, but the changing amplitude of GTs weakened progressively with increasing depth and varied significantly from one site to another (Fig. 3a). For example, the JS site with a high permafrost temperature had the maximum variation amplitude of GT at a depth of 0.5 m (from −14.9 to 16.6 °C) among all the five sites, while at the depth of 3 m, the XT site had the maximum variation amplitude of GT, which would be mainly related to local topography, vegetation, and geological condition (Table 1).

The GTs at depths of 8, 10, 15, and 20 m showed that permafrost temperature decreased with the increasing latitude. Overall, the relationship between GT and latitude is not linearly dependent (Fig. 3b). The seasonal changes

https://doi.org/10.5194/essd-2022-167
Preprint. Discussion started: 31 May 2022

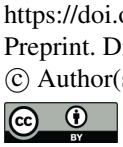

Open Access Earth System Science Data Discussions

191 of GTs at depths ⩾ 15 m at all sites are negligible except for the JS site, which indicates that zero annual amplitude
192 (ZAA) is located below 15 m in depth. At the JS site, abnormal positive temperatures were observed in summers of
193 2019 and 2020, probably due to the thermal disturbance of intra-permafrost water.

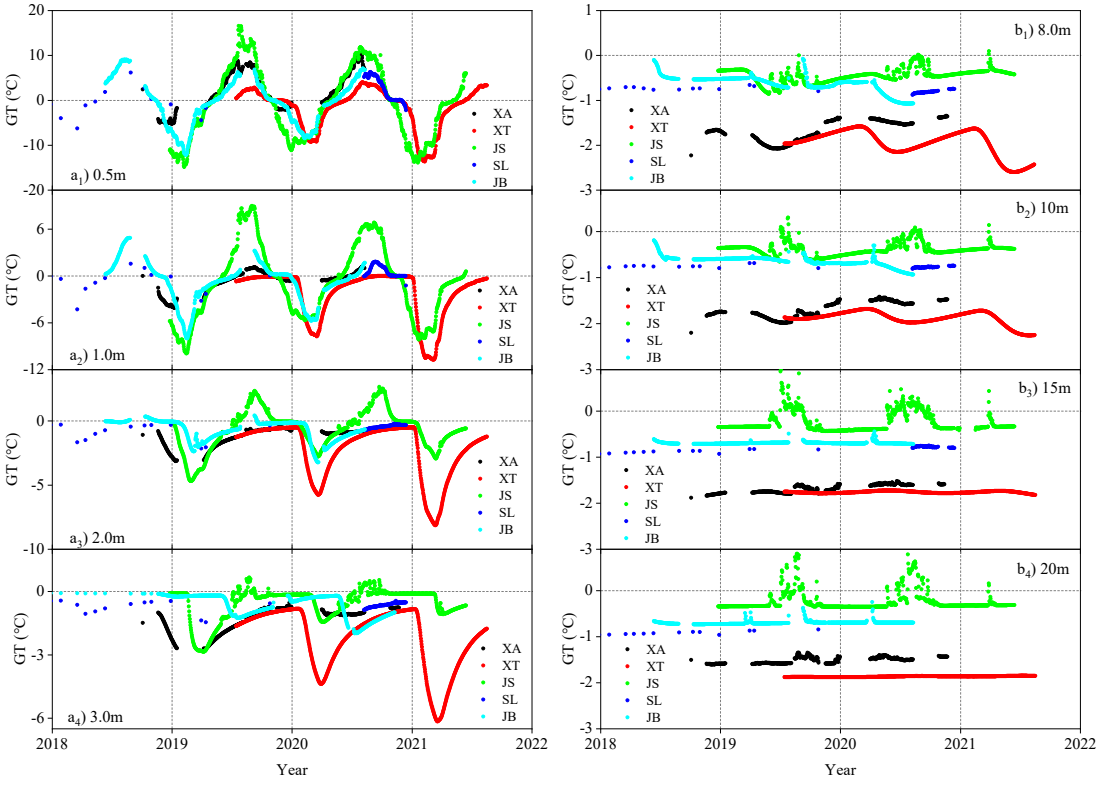

194

195 Figure 3. Variability of ground temperatures in the active layer (a) and permafrost (b) at the undisturbed sites along the
196 route of CRCOPs in Northeast China, 2018–2021.

197 A decade record (2011–2020) of GTs in the active layer and permafrost in borehole JB-B-II allows for
198 assessment of the inter-annual trend of permafrost under a warming climate. As displayed in Fig. 4, the monthly
199 average GTs in 2018 at depths from 1 to 2 m was fluctuating in proximity to 0 °C without an obvious geothermal
200 gradient (termed as the zero curtain layer), decreased with a geothermal gradient of 0.08 °C m^{-1} at depths from 2 to
201 7 m, and remained unchanged below 7 m. The ALT (the maximum depth of 0 °C isotherm from linear interpolation
202 of the daily average GTs) showed little variations in this borehole, varying between 178 and 200 cm from 2011 to

https://doi.org/10.5194/essd-2022-167
Preprint. Discussion started: 31 May 2022

2020 mainly due to the damping effect of the zero curtain layer (Fig. 5a), while the deeper permafrost (at depths from 8 to 20 m) was warming at an average rate of 0.035 °C yr^{-1} in this 10-year observation period (Fig. 5b). At the D_{ZZA} of 15 m, MAGT increased by 0.3 °C (from −0.8 to −0.5 °C).

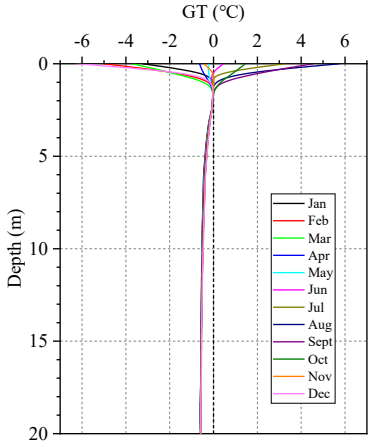

Figure 4. Monthly average ground temperatures at different depths in 2018 recorded in the JB-B-II borehole at the JB site.

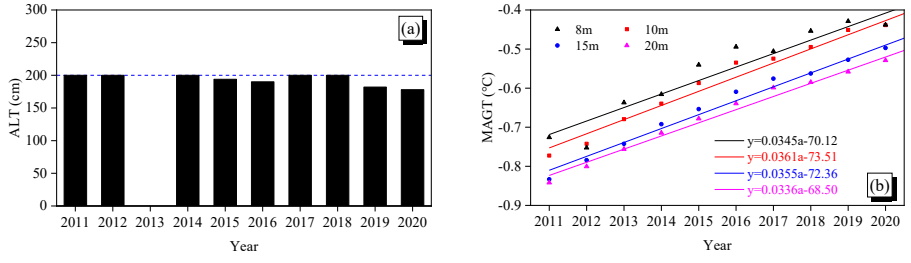

Figure 5. Variations in the active layer thickness (ALT) (a) and mean annual ground temperature (MAGT) (b) from 2011 to 2020 in borehole JB-B-II at the JB site.

3.3 Ground temperature on the ROW of pipeline

Boreholes on the ROW along the CRCOPs were drilled and instrumented for GT monitoring at three permafrost sites (JS, SL, and JB) to evaluate the thermal disturbances of the insulated or uninsulated CRCOPs on the surrounding permafrost (Table 3). At the JS and SL sites, the pipelines were insulated and initially buried at a depth of 2 m, while they were uninsulated and buried about 1.6 m in depth at the JB site. The warm oil (with the maximum recorded temperature of 28 °C at the first pump station of the CRCOPs in China) flowing in the pipeline brought substantial

https://doi.org/10.5194/essd-2022-167
Preprint. Discussion started: 31 May 2022

Open Access Earth System Science Data Discussions

heat into the underlying and ambient permafrost, resulting in the GT rising, even though the pipelines were wrapped by an insulation layer (Fig. 6). However, temperature differences on and off the ROW of pipeline were substantially reduced by an insulation layer at the JS and SL sites compared to those at the JB site. Besides, GT in the borehole 5 m (perpendicular to the CRCOP I) away from the pipe centerline was also greater than that at the nearby undisturbed site, indicating the lateral thermal disturbance range of the pipeline may have extended beyond 5 m.

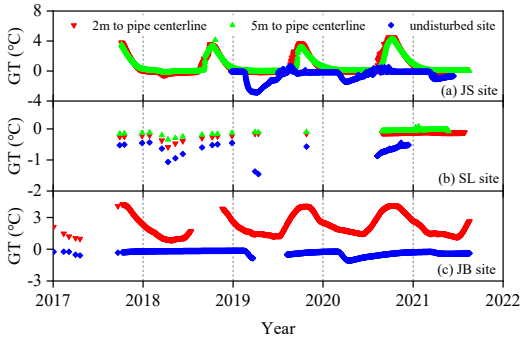

Figure 6. Variations in ground temperatures at the depth of 3 m on the ROW at the JS (a), SL (b), and JB (c) sites along the CRCOP I, 2017–2021.

The time-series of artificial permafrost table (APT) in borehole JB-B-1, 2 m away from the uninsulated pipe centerline at the JB site, shows that the APT has been increasing since the official operation of CRCOP I starting from 2011, with an average rate of 0.9 m yr^{-1} during 2010–2020 (Fig. 7). This has demonstrated that the pipeline has triggered an intensive and quick permafrost degradation at a local scale. This deepening of the permafrost table and warming of permafrost has exposed the pipelines to thawed low-bearing foundation soils, resulting in potential pipeline damage. For example, the excavation at the JB site in 2015 revealed that the CRCOP I had locally settled by 1.4 m during 2010–2015.

The inverted ERT results, i.e., distribution of apparent ER within the subsurface, can provide information regarding the spatial distribution of permafrost and taliks (thawed or unfrozen zones in permafrost regions). The configurations of talik around the CRCOPs can be seen in Figure 8. Here, an ER value of 300 Ωm is used for interpreting the boundary combined with the profile characteristics of resistivity, GT, water/ice content, and lithology

https://doi.org/10.5194/essd-2022-167
Preprint. Discussion started: 31 May 2022

(obtained from borehole drilling). There is a significant difference in the sizes of taliks around the CRCOPs in April 2018, suggesting that pipeline operation-related thermal disturbances have accelerated permafrost thaw (Fig. 8). Besides, the shallow soil layer beneath the cleared pipeline ROW has a lower ER, compared to that in the adjacent undisturbed site at the same time (Fig. 8), indicating that the clearing of the ROW has also contributed to permafrost warming and thawing.

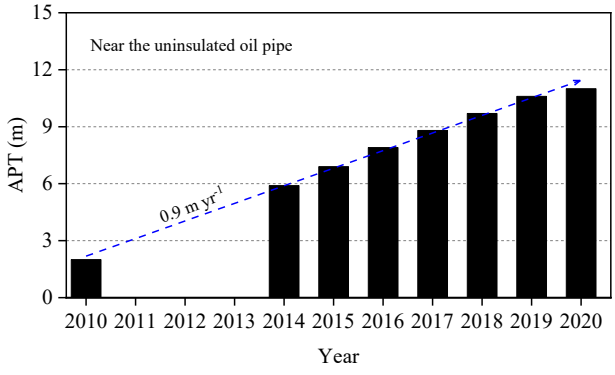

Figure 7. Variations in the artificial permafrost table (APT) during 2010–2020 in borehole JB-B-1, 2 m away from the centerline of the uninsulated CRCOP I at the JB site.

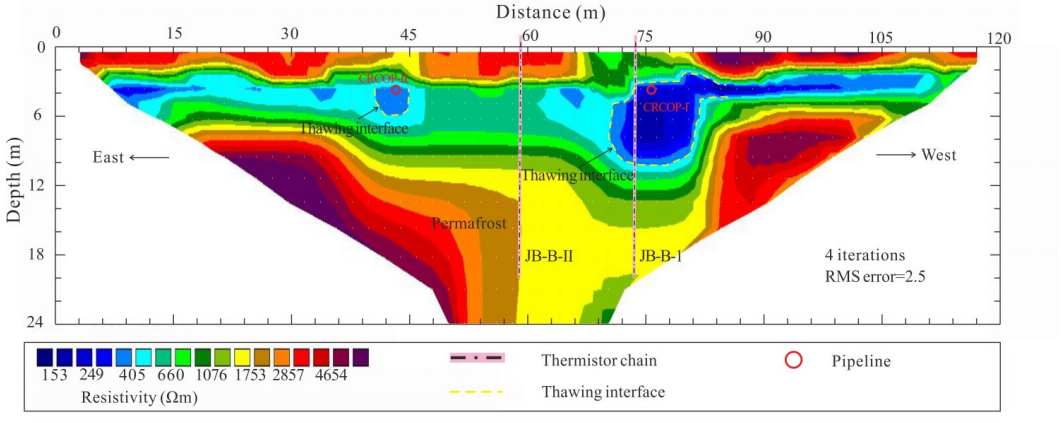

Figure 8. Inversion results of electrical imaging along P-JB-1 profile at the JB site, carried out in April 2018.

The two-phase closed thermosyphons (TPCTs), a widely-used mitigative measure for permafrost thaw in cold region engineering, will locally change the temporal and spatial variations of GT distribution. Figure 9 shows the

https://doi.org/10.5194/essd-2022-167
Preprint. Discussion started: 31 May 2022

248 time series of temperature contours in boreholes of JB-B-2, JB-B-3, JB-B-6, and JB-B-9 from July 2015 to August
249 2021 (the period with high-quality GT data series). Borehole JB-B-2 is located 2 m away from the pipeline centerline
250 with one pair of TPCTs, while boreholes JB-B-3, JB-B-6, and JB-B-9 are set 2, 3, and 4 m respectively away from
251 the centerline of the CRCOP I with two pairs of TPCTs. During the cold season, APT remains unchanged due to the
252 cooling effect of TPCTs, but it deepens when the TPCTs stop working during the warm season. Overall, APT has
253 been increasing slowly over the observational decade (Fig.9a). The cooling performance of the TPCTs on pipeline
254 foundation soils has been enhanced with an increased number of TPCTs, as characterized by a slower rate of APT
255 deepening and a wider vertical cooling extent (Fig.9b). Besides, GTs in boreholes of JB-B-6 and JB-B-9 indicate a
256 greater-than-1.5-m the cooling range of TPCTs, and a greater-than-4-m lateral extent on the ground surface of thermal
257 disturbance of the warm pipeline (CRCOP I) (Fig.9c and 9d). During June–August 2020, abnormal changes in 0 °C
258 isotherm observed in Figures 9b, 9c, and 9d are likely related to the infiltration of surface water and/or intra-
259 permafrost water. The above results show that the vertically-inserted TPCTs are unable to completely control the
260 thawing of permafrost underlying the pipeline. The unexpectedly warmer oil temperature, thermal erosion of surface
261 water ponding on the ROW, degrading TPCT performance, as well as climate warming are responsible for the
262 unsatisfactory cooling effect of TPCTs on the pipeline foundation soils.

https://doi.org/10.5194/essd-2022-167
Preprint. Discussion started: 31 May 2022

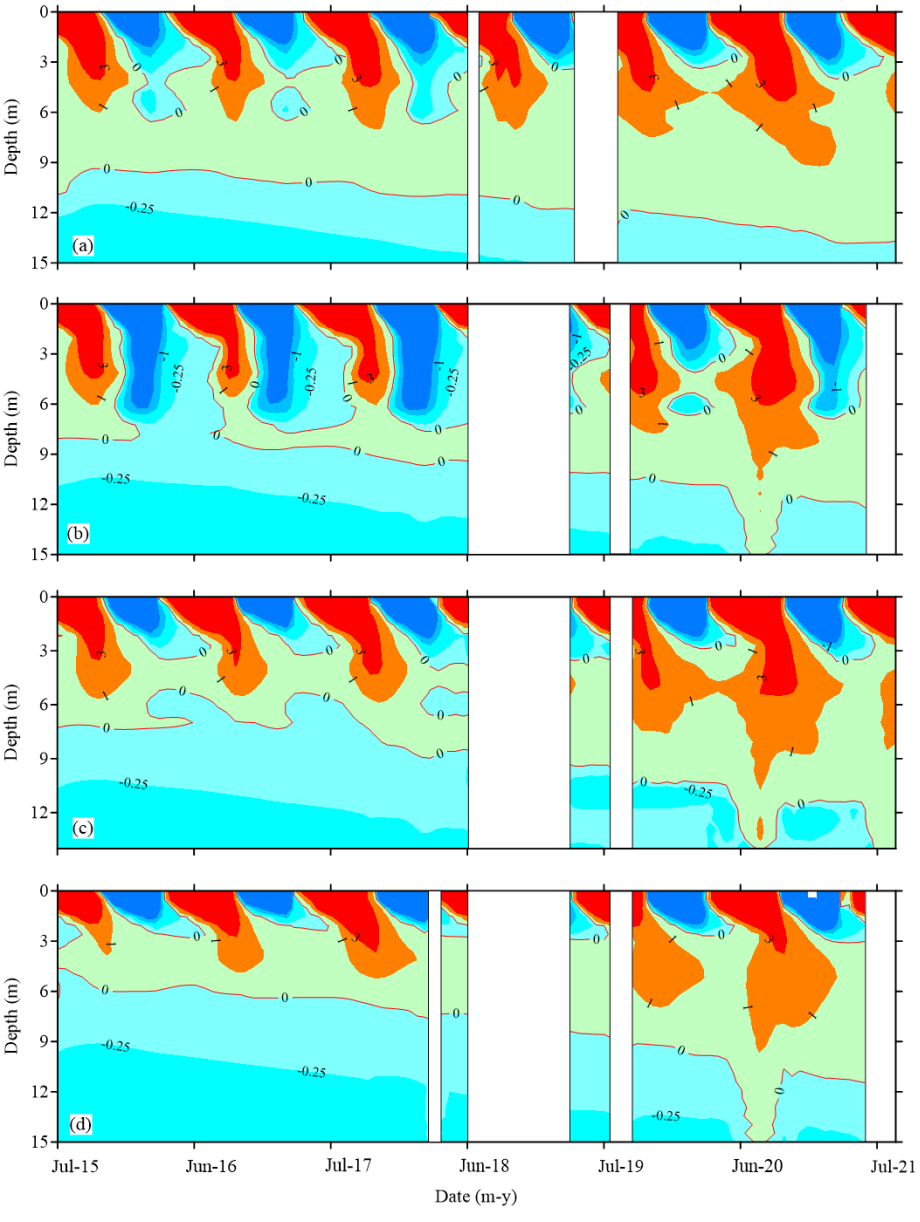

Figure 9. Time series of temperature contours (°C) with TPCTs from the ground surface (0 m) to a depth of 15 m, derived from the boreholes JB-B-2 (a), JB-B-3 (b), JB-B-6 (c), and JB-B-9 (d) at the JB site. The blank gap indicates the missing data.

The variations in VWC at depths of 0.5 m (peaty soil) and 1.5 m (silt clay) are controlled by the freeze-thaw processed of soil layers. In the thawing season, the VWC is 0.55 m^3 m^{-3} at 0.5 m and reaches 0.64 m^3 m^{-3} at 1.5 m.

https://doi.org/10.5194/essd-2022-167
Preprint. Discussion started: 31 May 2022

While the VWC at 2.5 m (silt clay) is less changed with an average of 0.45 m^3 m^{-3} (Fig.10), offering indirect evidence to the presence of talik around the warm-oil pipe (Li et al., 2018). All these findings undoubtedly confirm that the construction and operation of the buried warm pipeline have resulted in locally intensive thermal disturbances on the underlying permafrost in the ROW along CRCOP I, although spatially confined.

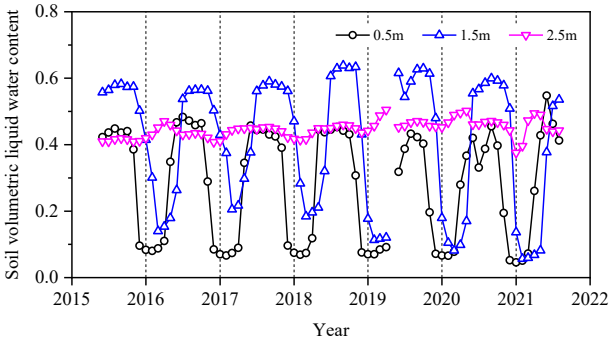

Figure 10. Temporal history of soil volumetric liquid water content at depths of 0.5, 1.5, and 2.5 m at the JB site.

4 Data availability

The data sets presented herein can be freely downloaded from the National Tibetan Plateau/Third Pole Environment Data Center at http://doi.org/10.11888/Cryos.tpdc.272357 (Li, 2022).

5 Conclusions

For this study, an in-situ monitoring network for the ground thermal state was established along the CRCOP route, at the eastern flank of the northern Da Xing'anling Mountains in Northeast China. The resulting dataset fills the gaps in the spatial coverage of high-latitude permafrost databases with and without warm pipeline disturbance. This dataset consists of daily ground temperatures at different depths in 20 boreholes (10 to 60.6 deep, spanning a range of latitudes from 50.47 to 53.33°N), soil volumetric liquid water contents, meteorological variables, and ERT data. The harsh environmental conditions and inaccessibility to the field sites during the COVID-19 pandemic have resulted in some missing data, but we will continue to update the dataset by overcoming these difficulties in subsequent years.

https://doi.org/10.5194/essd-2022-167
Preprint. Discussion started: 31 May 2022

The dataset presented herein shows permafrost at the eastern flank of the northern Da Xing'anling Mountains is controlled by latitude and strongly influenced by the local geo-environmental factors. The MAGT at 15 m ranges from −1.8 to −0.4 °C, and the ALT varies from 100 to 270 cm. The record from 2011 to 2020 of GT measurements indicates that ground warming has been extensively observed in the vicinity of the southern limit of latitudinal permafrost. The GT in deeper permafrost (8–20 m) has been rising at a rate of 0.035 °C yr^{-1}, but there is no significant change in ALT, varying between 178 and 200 cm within the 10-year observation period. The GT measurements on the ROW of pipeline and ERT results show that the construction and operation of the CRCOP have brought strong thermal disturbances to the underlying permafrost foundation soils, leading to a talik with a maximum depth of 11.5 m, although laterally much confined to the ROW of the CRCOP I. This permafrost disturbance is still in rapid expanding. Thawing of permafrost on the ROW of the pipeline cannot be completely prevented by installing the insulation layer or TPCTs, but its rate can be reduced significantly. This dataset provides a basis for assessing the spatio-temporal variability of permafrost under the linear disturbance of the buried warm pipeline and related environmental effects, for revealing hydro-thermal-mechanical interactions between buried pipeline and the ambient permafrost environment, for evaluating the integrity of the pipeline systems, and for consulting on the design and building of similar pipelines in permafrost regions.

Author contribution

GY, WM and HJ designed this study and obtained the financial support for establishing and maintaining the monitoring sites. FW and GY compiled the dataset, performed the analysis, and wrote the manuscript. FA, YH, and DC improved the writing. GW, YP, YZ, YC, JZ, KG, RH, XJ, XL, and YL participated in the fieldwork.

Competing interests

The authors declared no conflicts of interest in this work.

https://doi.org/10.5194/essd-2022-167
Preprint. Discussion started: 31 May 2022

Special issue statement

This article is part of the special issue "*Extreme environment datasets for the three poles*". It is not associated with a conference.

Acknowledgments

This work was financially supported by the Strategic Priority Research Program of Chinese Academy of Sciences (Grant No. XDA2003020102), the National Natural Science Foundation of China (Grant No. 42101121), and the Research Projects of the State Key Laboratory of Frozen Soil Engineering (Grant Nos. SKLFSE-ZY-20 and SKLFSE202010).

References

Beck I, Ludwig R, Bernier M, et al. Vertical movements of frost mounds in subarctic permafrost regions analyzed using geodetic survey and satellite interferometry[J]. Earth Surface Dynamics, 2015, 3(3): 409-421.

Biskaborn B K, Simth S L, Noetzli J, et al. Permafrost is warming at a global scale[J]. Nature Communications, 2019, 10: 264.

Brown J, Ferrians Jr O J, Heginbottom J A, et al. Circum-arctic map of permafrost and ground-ice conditions. National Snow and Ice Data Center/World Data Center for Glaciology, 1998.

Cheng G, Jin H. Permafrost and groundwater on the Qinghai-Tibet Plateau and in northeast China[J]. Hydrogeology Journal, 2013, 21(1): 5-23.

Dahlin T, Zhou B. A numerical comparison of 2D resistivity imaging with 10 electrode arrays[J]. Geophysical prospecting, 2004, 52(5): 379-398.

Farzamian M, Vieira G, Monteiro Santos F A, et al. Detailed detection of active layer freeze-thaw dynamics using quasi-continuous electrical resistivity tomography (Deception Island, Antarctica)[J]. The Cryosphere, 2020, 14(3):

https://doi.org/10.5194/essd-2022-167
Preprint. Discussion started: 31 May 2022

1105-1120.

Guo D, Li Z. Historical evolution and formation age of permafrost in northeastern China since the late Pleistocene[J]. Journal of Glaciology and Geocryology 3(4): 1-6. (In Chinese)

Guo W, Liu H, Anenkhonov O A, et al. Vegetation can strongly regulate permafrost degradation at its southern edge through changing surface freeze-thaw processes[J]. Agricultural and Forest Meteorology, 2018, 252: 10-17.

Harris C, Mühll D V, Isaksen K, et al. Warming permafrost in European mountains[J]. Global and Planetary Change, 2003, 39(3-4): 215-225.

Harris S A, Brouchkov A, Guodong C. Geocryology: characteristics and use of frozen ground and permafrost landforms[M]. CRC Press, 2017.

He R, Jin H, Luo D, et al. Permafrost changes in the Nanwenghe Wetlands Reserve on the southern slope of the Da Xing'anling–Yile'huli mountains, Northeast China[J]. Advances in Climate Change Research, 2021, 12(5): 696-709.

Hjort J, Karjalainen O, Aalto J, et al. Degrading permafrost puts Arctic infrastructure at risk by mid-century[J]. Nature communications, 2018, 9(1): 5147.

Hjort J, Streletskiy D, Doré G, et al. Impacts of permafrost degradation on infrastructure[J]. Nature Reviews Earth & Environment, 2022, 3(1): 24-38.

Isaksen K, Sollid J L, Holmlund P, et al. Recent warming of mountain permafrost in Svalbard and Scandinavia[J]. Journal of Geophysical Research: Earth Surface, 2007, 112(F2).

Jin H, Hao J, Chang X, et al. Zonation and assessment of frozen-ground conditions for engineering geology along the China–Russia crude oil pipeline route from Mo'he to Daqing, Northeastern China[J]. Cold Regions Science and Technology, 2010, 64: 213-225.

Jin H, Ma Q. Impacts of permafrost degradation on carbon stocks and emissions under a warming climate: A review[J]. Atmosphere, 2021, 12(11): 1425.

Jin H, Huang Y, Bense V F, et al. Permafrost degradation and its hydrogeological impacts[J]. Water, 2022, 14(3): 372.

https://doi.org/10.5194/essd-2022-167
Preprint. Discussion started: 31 May 2022

351 Jin H, Wu Q, Romanovsky V E. Degrading permafrost and its impacts[J]. Advances in Climate Change Research,
352 2021, 12(1): 1-5.
353 Jin H, Sun G, Yu S, et al. Symbiosis of marshes and permafrost in Da and Xiao Hinggan Mountains in northeastern
354 China[J]. Chinese Geographical Science, 2008, 18(1): 62-69.
355 Jin H, Yu Q, Lü L, et al. Degradation of permafrost in the Xing'anling Mountains, Northeastern China[J]. Permafrost
356 and Periglacial Processes, 2007, 18(3): 245-258.
357 Jones B M, Grosse G, Farquharson L M, et al. Lake and drained lake basin systems in lowland permafrost regions[J].
358 Nature Reviews Earth & Environment, 2022, 3(1): 85-98.
359 Koven C D, Riley W J, Stern A. Analysis of permafrost thermal dynamics and response to climate change in the
360 CMIP5 Earth System Models[J]. Journal of Climate, 2013, 26(6): 1877-1900.
361 Li G. Ground temperature dataset of permafrost along the China-Russia crude oil pipeline route (2011-2021),
362 National Tibetan Plateau Data Center[data set], http://doi.org/10.11888/Cryos.tpdc.272357, 2022.
363 Li G, Wang F, Ma W, et al. Field observations of cooling performance of thermosyphons on permafrost under the
364 China-Russia Crude Oil Pipeline[J]. Applied Thermal Engineering, 2018, 141: 688-696.
365 Li X, Jin H, Wang H, et al. Influences of forest fires on the permafrost environment: A review[J]. Advances in Climate
366 Change Research, 2021, 12(1): 48-65.
367 Liu W, Fortier R, Molson J, et al. Three-dimensional numerical modeling of cryo-hydrogeological processes in a
368 river-talik system in a continuous permafrost environment[J]. Water Resources Research, 2022: e2021WR031630.
369 Luo L, Zhuang Y, Zhang M, et al. An integrated observation dataset of the hydrological and thermal deformation in
370 permafrost slopes and engineering infrastructure in the Qinghai–Tibet Engineering Corridor[J]. Earth System Science
371 Data, 2021, 13(8): 4035-4052.
372 Mao Y, Li G, Ma W, et al. Field observation of permafrost degradation under Mo'he airport, Northeastern China from
373 2007 to 2016[J]. Cold Regions Science and Technology, 2019, 161: 43-50.

https://doi.org/10.5194/essd-2022-167
Preprint. Discussion started: 31 May 2022

374 Miner K R, Turetsky M R, Malina E, et al. Permafrost carbon emissions in a changing Arctic[J]. Nature Reviews
375 Earth & Environment, 2022, 3(1): 55-67.
376 Nelson F E, Anisimov O A, Shiklomanov N I. Subsidence risk from thawing permafrost[J]. Nature, 2001, 410(6831):
377 889-890.
378 Osterkamp T E, Romanovsky V E. Evidence for warming and thawing of discontinuous permafrost in Alaska[J].
379 Permafrost and Periglacial Processes, 1999, 10(1): 17-37.
380 Ran Y, Li X, Cheng G, et al. Distribution of permafrost in China: an overview of existing permafrost maps[J].
381 Permafrost and Periglacial Processes, 2012, 23(4): 322-333.
382 Ran Y, Li X, Cheng G. Climate warming over the past half century has led to thermal degradation of permafrost on
383 the Qinghai–Tibet Plateau[J]. The Cryosphere, 2018, 12(2): 595-608.
384 Serban R D, Serban M, He R, et al. 46-year (1973–2019) permafrost landscape changes in the hola basin, northeast
385 china using machine learning and object-oriented classification[J]. Remote Sensing, 2021, 13(10): 1910.
386 Schuur E A G, Vogel J G, Crummer K G, et al. The effect of permafrost thaw on old carbon release and net carbon
387 exchange from tundra[J]. Nature, 2009, 459(7246): 556-559.
388 Smith S L, O'Neill H B, Isaksen K, et al. The changing thermal state of permafrost[J]. Nature Reviews Earth &
389 Environment, 2022, 3(1): 10-23.
390 Turetsky M R, Abbott B W, Jones M C, et al. Carbon release through abrupt permafrost thaw[J]. Nature Geoscience,
391 2020, 13(2): 138-143.
392 Wang F, Li G, Ma W, et al. Permafrost warming along the Mo'he-Jiagedaqi section of the China-Russia Crude Oil
393 Pipeline[J]. Journal of Mountain Science, 2019a, 16(2): 285-295
394 Wang F, Li G, Ma W, et al. Pipeline–permafrost interaction monitoring system along the China–Russia crude oil
395 pipeline[J]. Engineering Geology, 2019b, 254: 113-125.
396 Wang Y, Jin H, Li G, et al. Secondary geohazards along the operating Mohe-Jagdaqi section of China-Russia crude

https://doi.org/10.5194/essd-2022-167
Preprint. Discussion started: 31 May 2022

397 oil pipeline in permafrost regions: a case study on a seasonal frost mound at the Site MDX364[J]. Journal of
398 Glaciology and Geocryology, 2015, 37(3): 731-739. (In Chinese)
399 Wei Z, Jin H, Zhang J, et al. Prediction of permafrost changes in Northeastern China under a changing climate[J].
400 Science China Earth Sciences, 2011, 54(6): 924-935.
401 Wu Q, Zhang T. Recent permafrost warming on the Qinghai-Tibetan Plateau[J]. Journal of Geophysical Research:
402 Atmospheres, 2008, 113(D13).
403 Wu T, Xie C, Zhu X, et al. Permafrost, active layer, and meteorological data (2010–2020) at the Mahan Mountain
404 relict permafrost site of northeastern Qinghai–Tibet Plateau[J]. Earth System Science Data, 2022, 14(3): 1257-1269.
405 Zhang Y, Chen W, Riseborough D W. Transient projections of permafrost distribution in Canada during the 21st
406 century under scenarios of climate change[J]. Global and Planetary Change, 2008, 60(3-4): 443-456.
407 Zhang Z, Wu Q, Hou M, et al. Permafrost change in Northeast China in the 1950s–2010s[J]. Advances in Climate
408 Change Research, 2021, 12(1): 18-28.
409 Zhao L, Zou D, Hu G, et al. A synthesis dataset of permafrost thermal state for the Qinghai–Tibet (Xizang) Plateau,
410 China[J]. Earth System Science Data, 2021, 13(8): 4207-4218.

https://doi.org/10.5194/essd-2022-167
Preprint. Discussion started: 31 May 2022

411 **Appendix A: Abbreviations**

ALT	Active layer thickness
APT	Artificial permafrost table
CRCOP	China-Russia crude oil pipeline
ER	Electrical resistivity
ERT	Electrical resistivity tomography
GT	Ground temperature
MAAT	Mean annual air temperature
MAGT	Mean annual ground temperature
ROW	Right-of-way
SLLP	Southern limit of latitudinal permafrost
TPCT	Two-phase closed thermosyphon
VWC	Volumetric liquid water content
ZAA	Zero annual amplitude

412 **Appendix B: Photos of meteorological station and instrumentations**

413
414 Figure B1. Jiabei automated weather station and instrumentations. Photo taken on April 2018. The rain gauge sensor has
415 been installed but is ineffective. The photo shows the location of the Jagdaqi pump station. The CR3000 data logger,
416 multiplexer, battery cell, solar charge controller, and wireless transmission module are placed in the white box with a solar
417 panel (i.e. insulated box). All monitoring devices are protected by an aluminum alloy fence.

https://doi.org/10.5194/essd-2022-167
Preprint. Discussion started: 31 May 2022

Open Access Earth System Science Data Discussions

418 **Appendix C: Relative position of boreholes and automatic collection instrumentation for ground temperatures**
419 **at permafrost monitoring sites**

420
421 Figure C1. Position of boreholes drilled on and off the pipeline ROW and the ERT profile at the JS permafrost site. Photo
422 taken on 29 June 2021. Ground temperatures are measured using thermistor chains connected to the CR3000 data logger.
423 (a) Wireless transmission module (HKT-DTU, Campbell Scientific, Inc., USA), (b) CR3000 data logger with a TRM128
424 multiplexer, (c) Solar charge controller (Phocos ECO (10 A), Germany), (d) Battery cell, a part of the power supply device.

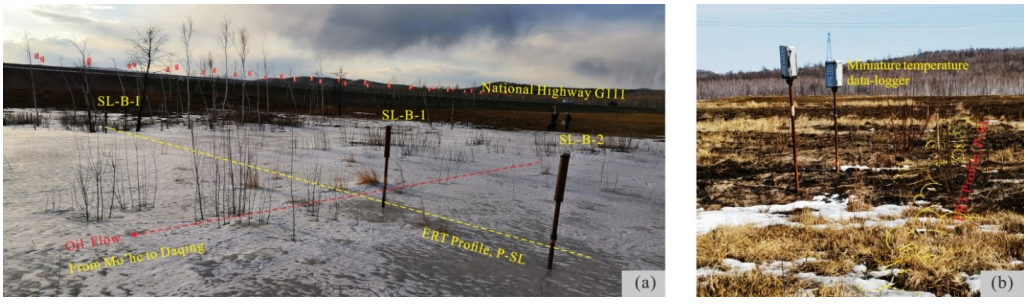

425
426 Figure C2. (a) Position of boreholes drilled on and off the pipeline ROW and the ERT profile at the SL permafrost site.
427 Photo taken on 30 March 2018. The ground surface within the trench is completely covered with ice and snow. (b) Miniature
428 temperature data loggers were installed in August 2020. Photo taken on 17 April 2021. The surface vegetation is destroyed
429 by manual-controlled fire.

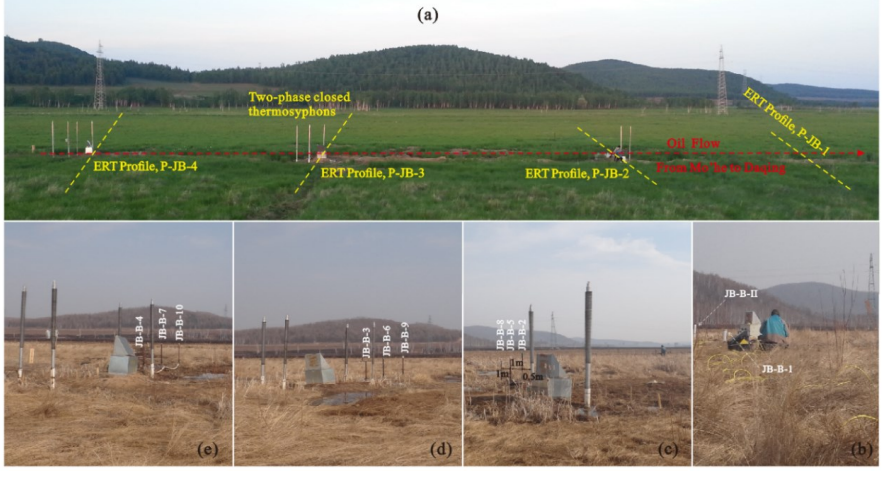

430

https://doi.org/10.5194/essd-2022-167
Preprint. Discussion started: 31 May 2022

Figure C3. Picture of the monitored cross-sections, perpendicular to the pipeline at 20 m intervals, at the JB permafrost site. (a) Plane view, (b) section 1, without TPCT, (c) section 2, one pair of TPCTs, (d) section 3, two pairs of TPCTs at a longitudinal spacing of 1.3 m, (e) section 4, two pairs of TPCTs at a longitudinal spacing of 1.4 m. The data acquisition device is the same as that at the JS site.

Appendix D: ERT results along P-JS, P-SL, P-JB-2, P-JB-3, and P-JB-4 profiles

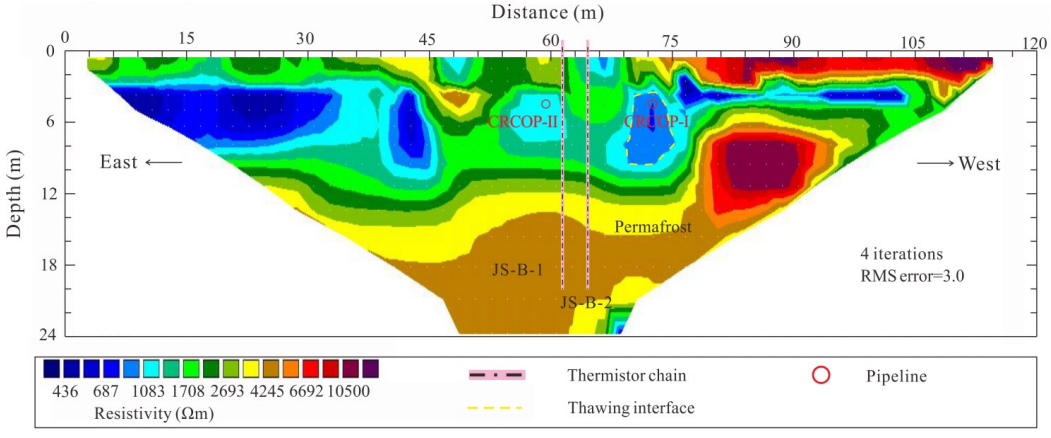

Figure D1. Inversion results of electrical imaging along P-JS profile at the JS site, carried out in April 2018.

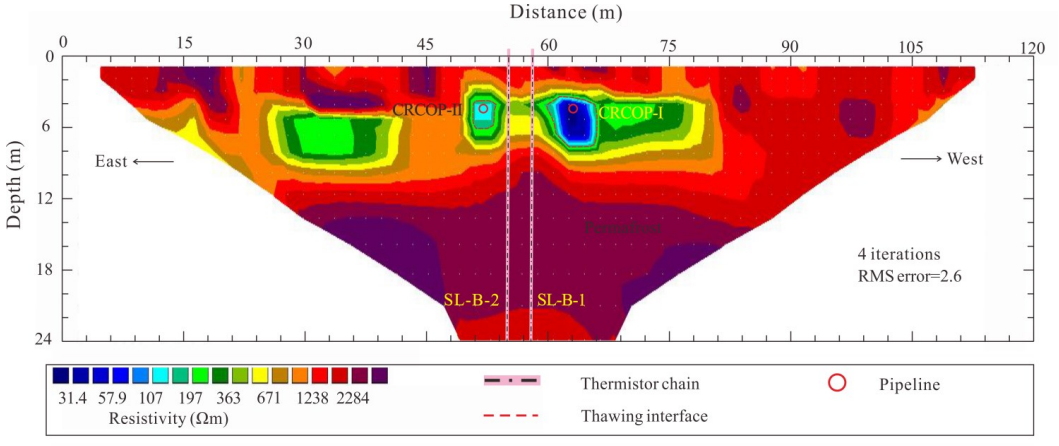

Figure D2. Inversion results of electrical imaging along P-SL profile at the SL site, carried out in April 2018.

https://doi.org/10.5194/essd-2022-167
Preprint. Discussion started: 31 May 2022

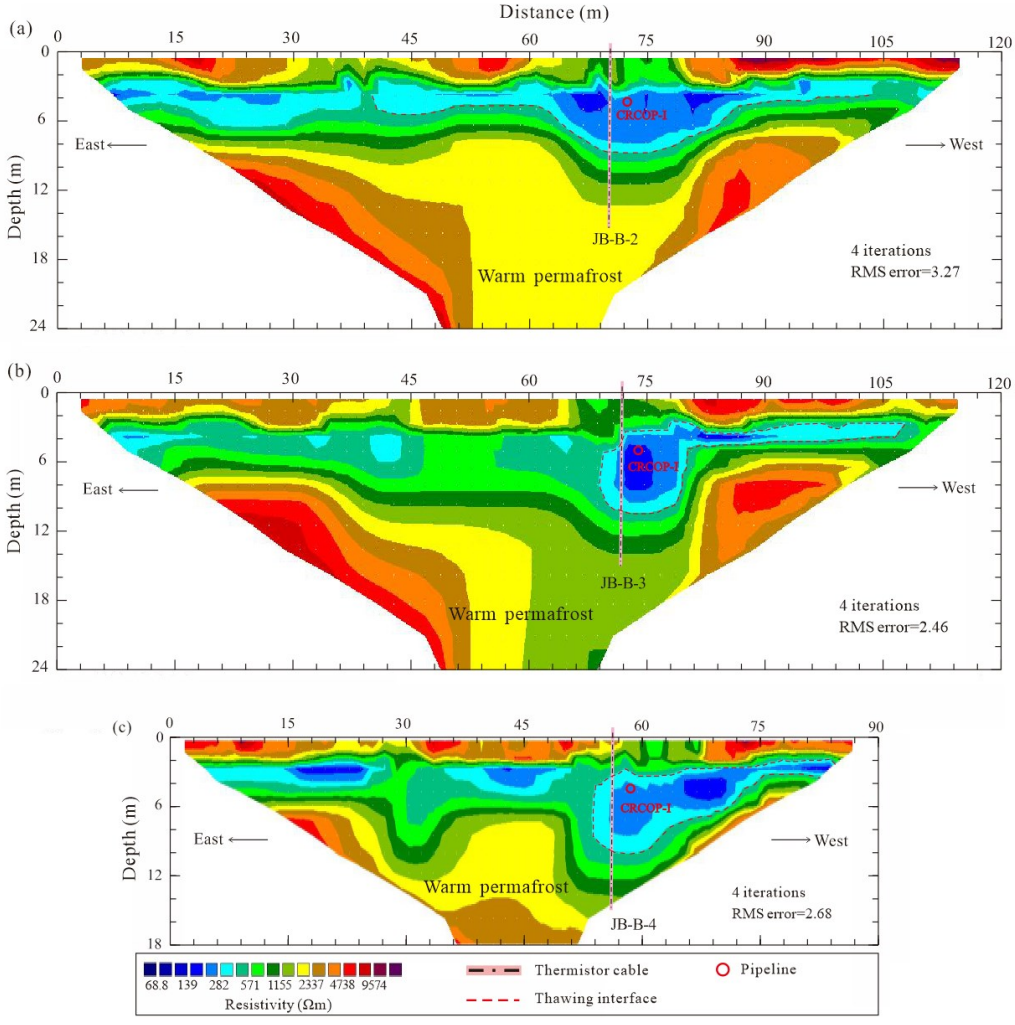

Figure D3. Inversion results of electrical imaging along monitored cross-sections with TPCTs at the JB site, carried out in April 2018. (a) P-JB-2 profile , one pair of TPCTs, (b) P-JB-3 profile, two pairs of TPCTs at a longitudinal spacing of 1.3 m, and (c) P-JB-4 profile , two pairs of TPCTs at a longitudinal spacing of 1.4 m.